ACS OMEGA

Open Access

http://pubs.acs.org/journal/acsodf

Article

Cracking Behavior and Stress Field Evolution in Coal Specimens Containing Bedding under Uniaxial Compression

Chang Guo, Zedong Wang, Ting Liu, Baiquan Lin, Chuanjie Zhu, Zhanbo Huang, and Nan Liu*

Cite This: *ACS Omega* 2023, 8, 37202−37212

Read Online

ACCESS | Metrics & More | Article Recommendations

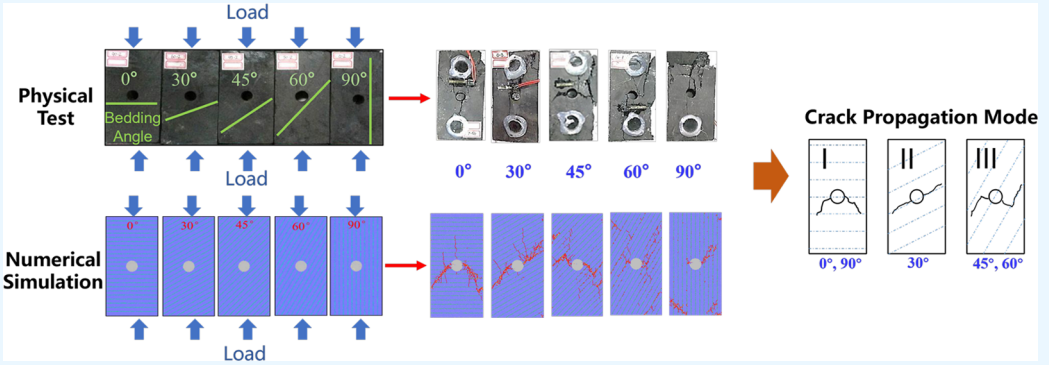

ABSTRACT: During the underground mining process, various coal seams with different bedding structures are often encountered. The presence of bedding structures is one of the primary factors that influence the strength and deformation characteristics of the coal seam and then affect gas extraction and gas disaster prevention. However, there is still a lack of mechanical properties of coal rock with structural anisotropy influenced by bedding structures. In this study, numerical models were established by using the particle flow code method to simulate coal specimens containing bedding with varying inclination angles. The results demonstrate the impact of the bedding inclination angle on the mechanical properties, crack propagation patterns, and the temporal and spatial evolution of the stress field in coal specimens with bedding during the loading process. Furthermore, three crack initiation patterns were investigated for coal specimens with different bedding angles. Additionally, the quantitative relationship between the mechanical properties and the fractal dimension was analyzed. The numerical simulation results were effectively validated through laboratory tests.

1. INTRODUCTION

Gas-related disasters associated with coal mining have long been a significant challenge, impeding the safety of coal mine production.[1−3] Gas extraction serves as a crucial technological approach for preventing and utilizing gas in coal mines.[4−7] The strength, deformation, and permeability of the coal seam play a vital role in determining the effectiveness of gas extraction in coal mines.[8−10]

A coal seam is a representative sedimentary rock consisting of coal particles, pores, fissures, and clay.[11] Over long geological periods, various structural planes such as bedding, fissures, and faults form within the coal seam due to geological tectonic processes.[12,13] Among these structures, bedding is the most widespread and exerts a decisive influence on the stability, recoverability, and gas flow conditions of the coal seam.[14−16] The presence of bedding structure is a key factor impacting the strength and deformation characteristics of the coal seam, resulting in complex discontinuities, heterogeneity, and strong anisotropy in the coal seam, as well as altering its stress state.[17−19] Consequently, studying the evolution of damage characteristics in coal-containing bedding holds practical value in understanding the mechanical deformation and damage features of coal with bedding while also enhancing gas extraction efficiency.[20] Furthermore, it offers theoretical support and a scientific foundation for comprehending the mechanisms behind various dynamic disasters in the coal seam, providing effective early warning of disasters, and implementing prevention and control measures.[21]

Coal is a geological material that undergoes various geological tectonic processes during its formation, leading to the transformation of intact coal rock into a geological body with varying degrees of damage, such as noticeable bedding

Received: July 6, 2023
Accepted: September 12, 2023
Published: September 29, 2023

structures.[22] The presence of bedding structures significantly influences the mechanical properties of coal rock, including compressive strength, elastic modulus, and cohesion, resulting in apparent anisotropic characteristics.[23] Scholars and experts have dedicated considerable attention to studying the mechanical properties of coal-containing bedding. In 1960, Jaeger introduced the concept of strength anisotropy in coal, attributing it to the effect of a single weak plane, laying the foundation for the study of coal anisotropy.[24] Subsequently, many scholars expanded and refined the theory through further research.[25] Hoek and Brown analyzed the anisotropic strength curves of rock materials with one set of joints and two sets of orthogonal joints.[26] Shi developed a prediction model for the anisotropic strength of layered rocks consisting of two parameters: the orientation of minimum strength and the anisotropy effect in layered rocks. The proposed model can be usefully applied to strength estimations of anisotropic rocks using the minimum amount of available test data.[27] Tests conducted by Alexeeva and Okubo revealed that the failure strength of coal under direct uniaxial tension was only one-third to one-half of the uniaxial tensile strength measured through fracturing tensile tests. Additionally, the elastic modulus of coal under direct uniaxial tension was significantly smaller than that under uniaxial compression.[28,29] Song et al. explored microstructure-related effects of the loading direction and specimen size on the anisotropy of uniaxial compressive strength in coal. They found the degree of the strength anisotropy decreases with increasing specimen size because of the enhanced microstructural volume of a larger specimen.[30]

These research findings reveal significant disparities in the mechanical properties of coal based on the different bedding directions. Under the influence of the bedding structure, the mechanical parameters of coal, including compressive strength and modulus of elasticity, exhibit variations corresponding to changes in the bedding dip angle, thus displaying clear anisotropic characteristics. However, the original stress balance in the coal seam is broken after drilling. The coal around the drilling is destroyed, and the strength and deformation characteristics of the coal are also changed. Lots of research results on the mechanical behavior characteristics of the complete coal affected by mining have been made, but there are still few reports on the research on the damage evolution characteristics of the coal after extraction drilling based on the bedding structure. There remains a dearth of systematic and in-depth investigations regarding qualitative and quantitative analyses, as well as physical and numerical combined experiments, on the mechanical properties of coal rock with structural anisotropy affected by the bedding structure. Therefore, coal samples with boreholes were selected to analyze the influence of the bedding structure on the strength and deformation characteristics of coal with boreholes.

2. RESEARCH METHODS

Uniaxial compression tests were conducted in the laboratory to investigate the mechanical properties of the borehole specimens. Additionally, numerical simulation methods were utilized to explore the mechanical mechanisms and validate the experimental results.

2.1. Laboratory Test. *2.1.1. Test Specimens.* The laboratory tests utilized raw coal from the Hongliu Coal mine in Shaanxi Province. The specimen size was 60 × 30 × 120 mm^3. The parameters of coal samples are shown in Table 1. The preparation process for specimens with different bedding inclination angles proceeded as follows. First, irregular raw coal blocks with noticeable bedding inclination structures were chosen and sliced into 30 mm thick sections along the vertical direction of the bedding, resulting in parallel beddings on the coal slices. Subsequently, the slices were further cut into 60 × 30 × 120 mm^3 coal specimens, maintaining angles of 0, 30, 45, 60, and 90°, respectively, to their bedding direction. Ultimately, three coal specimens were selected for each bedding inclination angle with a drilling diameter of 14 mm. Additionally, all end faces of the coal specimens were meticulously polished and smoothed.

Table 1. Parameters of the Coal Samples

coal sample	M_{ad} (%)	A_d (%)	V_{daf} (%)	FC_d (%)
Hongliu	8.68	10.6	37.36	57.79

2.1.2. Test Methods and Apparatus. Uniaxial loading experiments were conducted on coal specimens to examine the influence of different bedding structures on their mechanical properties. The loading direction is along the axis of the coal specimen. The loading rate was set at 0.2 mm/min, and the stress−strain curve, uniaxial compressive strength (UCS), and elastic modulus (E) of each specimen were carefully monitored. A digital camera was employed to capture the loading processes and observe the initiation, propagation, and coalescence of cracks within the specimens. To minimize experimental errors arising from sample variability, we repeated each test three times. Figure 1 illustrates the arrangement of strain gauges on the specimens.

Figure 1. Strain gauges on the specimens.

2.2. Numerical Simulation. *2.2.1. Brief Introduction of Particle Flow.* The mechanical behaviors of a particle assembly composed of nonuniform-sized circular particles bonded together at the contact points are simulated using the bonded particle model (BPM).[31] The motion of the particles follows Newton's second law, while the interaction between particles adheres to the law of force−displacement. The BPM consists of two microbond models: the contact bond model and the parallel bond model,[32] as illustrated in Figure 2. The contact bond model transfers force exclusively, whereas the parallel bond model can simultaneously transfer both moment and force.

https://doi.org/10.1021/acsomega.3c04849
ACS Omega 2023, 8, 37202−37212

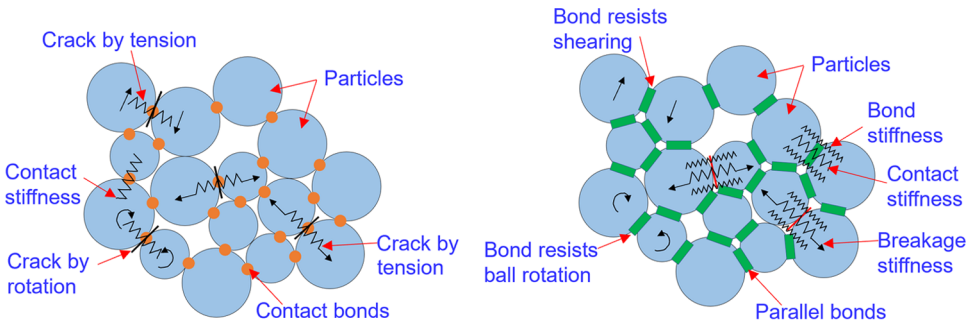

(a) Contact bonding model (b) Parallel bond model

Figure 2. Particle bond model: (a) contact bonding model; (b) parallel bond model.

Table 2. Mesoscopic Mechanic Parameters of Parallel Bond Model[33,34]

particle parameters	particle density (kg/m^3)	particles connect modulus (GPa)	stiffness ratio of particles (k_n/k_s)	friction coefficient of particles	particle radius ratio	minimum particle radius (mm)
value	1635	2.4	1.0	0.7	1.66	1.7
parallel bonding parameters	normal bond strength (MPa)	normal bond strength deviation (MPa)	tangential bond strength (MPa)	tangential bond strength deviation (MPa)	bonding radius multiplier λ	parallel bond stiffness ratio (k_n/k_s)
value	7	0.1	7	0.1	1.0	1.0

Several scholars suggest that the parallel bond model is better suited for simulating the mechanical properties of coal materials and analyzing the evolution of damage characteristics in coal materials from a micromechanical perspective.

2.2.2. Calibration of Mesoscopic Parameters. To create a parallel bond model, it is essential to establish a set of mesoscopic parameters. In this study, a numerical model was developed using the particle flow code in two dimensions (PFC^{2D}) to simulate laboratory test specimens with dimensions of 60 × 120 mm^2 and a size ratio of 1:1. The particles in the model were randomly generated based on a uniform distribution and bonded together using parallel bonding. The meso-parameters of the model were determined by synthesizing previous research findings and uniaxial experimental results obtained from coal specimens at the experimental scale.[32] A summary of these parameters is presented in Table 2.

To consider the variations in the inclination of the stratified structural plane of coal, a numerical model was constructed for layered coal with different bedding angles, employing the mesomechanical parameters specified in Table 2. The numerical simulation scheme was devised as follows.

A circular hole with a radius of 14 mm was generated at the center of the numerical specimen. The research focused on layered coal bodies containing boreholes with bedding inclination angles of 0, 30, 45, 60, and 90°, as depicted in Figure 3. The loading direction is along the axis of the coal specimen. The objective of this study is to examine the impact of coal bedding structure anisotropy on mechanical characteristics, stress distribution around the borehole, crack propagation, and other damage and failure characteristics of excavated coal.

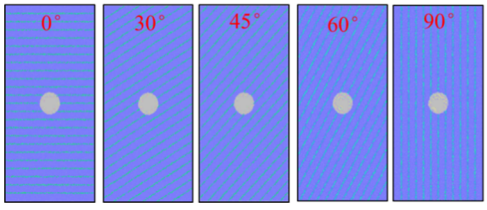

Figure 3. Numerical model of the coal specimen.

2.2.3. Specimens and Method. The axial or wall stress in the model was determined by dividing the average total force exerted by particles on the walls by the cross-sectional area of the specimen. The maximum axial stress corresponds to the UCS, while the slope of the linear portion of the stress−strain curve represents the elastic modulus. To maintain quasi-static equilibrium during computation, a loading rate of 0.2 mm/min was applied. This loading rate (<0.08 m/s), as indicated by Zhang and Wong,[35] is reasonable for static load analysis using the bonded particle model. To obtain a steady-state solution with a reasonable number of cycles, local damping with a damping constant of 0.7 was implemented in the simulation. A density-scaling algorithm was used in the numerical calculations. Furthermore, in the simulation experiments, the specimen was subjected to a strain-controlled loading by controlling the bottom and top walls at a specified speed. The normal stiffness of the top and bottom walls was set equal to the average particle normal stiffness.[36]

3. RESULTS

3.1. Stress−Strain Curves of Specimens Containing Borehole. Figure 4 illustrates the stress−strain relationship of borehole specimens with a 0° bedding inclination angle, as observed in laboratory tests. The loading process of the coal sample can be divided into four stages based on the characteristics of the stress−strain curve. These stages include the initial damage due to compaction (OA section), the linear elastic deformation stage (AB section), the yield stress stage prior to the peak (BC section), and the residual stress stage following the peak (CD section). During the initial loading stage (OA section), the stress−strain curve exhibits an upward bend as the initial load causes the closure of original pores and tiny fractures in the coal. As the load progresses (AB section), the sample enters a linear elastic deformation stage, resulting in a linear increase in the stress−strain curve. With further external load increase (BC section), the sample transitions into a stage of yield deformation before reaching its peak intensity. The curve's

https://doi.org/10.1021/acsomega.3c04849
ACS Omega 2023, 8, 37202−37212

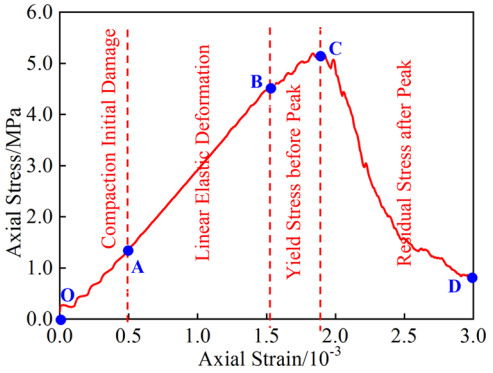

Figure 4. Stress−strain curve of bedded structure coal with uniaxial loading.

increasing tendency slows down due to the onset of plastic deformation. Once the peak intensity is reached, the curve gradually enters the stage of peak residual deformation (CD section). In this stage, the stress−strain curve decreases rapidly due to the pronounced deformation and destruction of the sample.

To investigate the impact of bedding on the mechanical properties of borehole specimens, axial stress−strain curves of borehole specimens were statistically generated through numerical simulations, considering both traditional bedding inclination angles and cases without considering them. The results are depicted in Figure 5, demonstrating significant

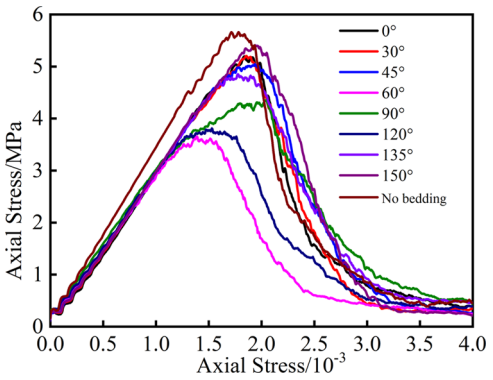

Figure 5. Axial stress-strain curve of borehole specimen with different bedding angles.

differences in the curves between the two scenarios. The findings indicate that specimens with larger inclination angles exhibit a higher peak strength (UCS). Additionally, the slope of the stress−strain curve segment gradually increases with an increase in the inclination angle, indicating that the elastic modulus also increases with the angle. These analyses collectively demonstrate a strong correlation between the mechanical properties of the borehole specimens and the bedding inclination.

3.2. Strength Characteristics of Specimens Containing Borehole. To determine the correlations between uniaxial compressive strength (UCS), elastic modulus, and bedding angle, a more detailed and quantitative analysis was performed in this section to explore the influence of the bedding angle on UCS and elastic modulus.

Figure 6 presents the relationship between the compressive strength of the borehole specimens and different bedding inclination angles. As illustrated in Figure 6, the compressive

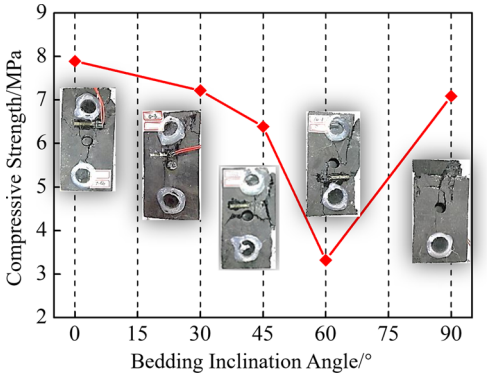

Figure 6. Compressive strength of experimental borehole specimen with the change of the bedding inclination angle.

strength of borehole specimens is influenced by the bedding structure. It gradually decreases initially and then increases with an increase in the bedding inclination angle.

Figure 7 illustrates the change in compressive strength of borehole specimens with varying bedding inclination angles by

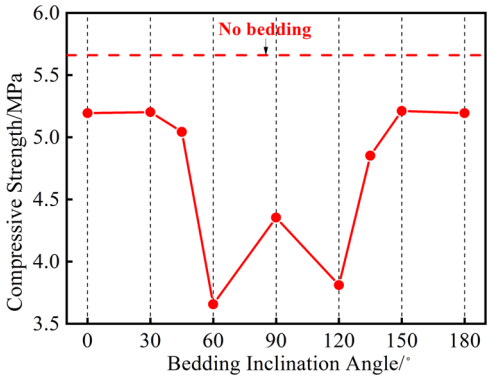

Figure 7. Variation of compressive strength of the borehole specimen with the bedding inclination angle.

numerical simulation. From the figure, it is evident that the compressive strength of the borehole specimen initially decreases and then increases within the range of 0−90° for the bedding inclination angle. Moreover, within the range of 0−180°, a symmetrical "W" shape distribution is observed around the 90° axis. This axisymmetric pattern arises from the inherent symmetry of the bedding structure. Furthermore, the numerical experiment confirms the variation pattern of compressive strength in borehole specimens with bedding inclination angles between 0−90°.

As depicted in Figure 7, the compressive strength of the borehole specimen gradually decreases with a slight slope as the bedding inclination angle increases within the range of 0−45°. The influence of the bedding structure on the compressive strength of the borehole specimen is not significantly pronounced within this range. Hence, the interval of bedding inclination angles from 0 to 45° can be defined as the zone of slow changes in compressive strength. However, within the range of 45 to 90° for the bedding inclination angle, the compressive strength curve of the borehole specimen exhibits considerable fluctuations. It undergoes a rapid decrease, followed by a rapid increase. The influence of the bedding structure on the compressive strength becomes evident on the left and right sides of this range. Consequently, the interval of

https://doi.org/10.1021/acsomega.3c04849
ACS Omega 2023, 8, 37202−37212

bedding inclination angles from 45 to 90° can be identified as the rapidly changing zone for compressive strength.

3.3. Deformation Characteristics of Specimens Containing Borehole. The elastic modulus values of the borehole specimen at bedding inclinations of 0, 30, 45, 60, and 90° are 1.02, 0.98, 0.86, 0.56, and 0.91 GPa, respectively. Figure 8 illustrates the curve depicting the change in the elastic modulus of the borehole specimen with varying bedding inclination angles. Within the range of 0−90°, the elastic modulus of the borehole specimen initially decreases and then increases with an increase in the bedding inclination angle. The maximum decrease is up to 45%, signifying that the structural heterogeneity of the bedding significantly impacts the deformation characteristics of the borehole specimen.

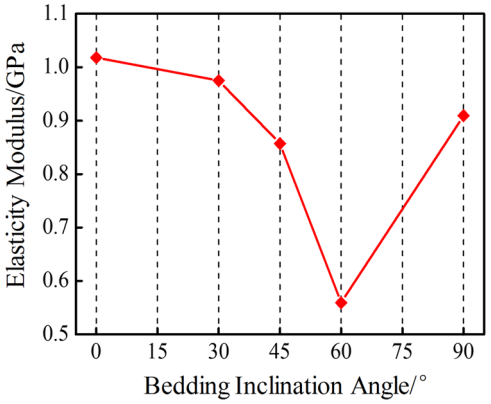

Figure 8. Elastic modulus of an experimental borehole specimen with the change in bedding inclination angle.

4. CRACK PROPAGATION PATTERNS IN SPECIMENS CONTAINING A BOREHOLE

The findings obtained from the analyses conducted reveal that specimens containing boreholes with different bedding angles exhibit distinct mechanical properties. It is widely recognized that the mechanical parameters of coal-rock masses are intimately linked to the processes of crack initiation, propagation, and coalescence within the specimens.[32,37−40] Therefore, it becomes essential to examine the patterns of crack propagation in specimens containing the combined flaws. Such an investigation will greatly contribute to an improved understanding of the mechanical properties involved.

Table 3 illustrates the crack propagation processes observed in specimens containing boreholes with various bedding angles

Table 3. Crack Propagation Processes of Specimens Containing Boreholes with Various Bedding Angles under Uniaxial Compression[a]

θ	Pre-peak		Peak	Post-peak		Physical Test
0°	(a) σ_i=0.71 σ_C	(b) σ_i=0.92 σ_C	(c) σ_i=σ_C	(d) σ_i=0.95σ_C	(e) σ_i=0.46σ_C	(f)
30°	(a) σ_i=0.67σ_C	(b) σ_i=0.93σ_C	(c) σ_i=σ_C	(d) σ_i=0.91σ_C	(e) σ_i=0.38σ_C	(f)
45°	(a) σ_i=0.47σ_C	(b) σ_i=0.89σ_C	(c) σ_i=σ_C	(d) σ_i=0.92σ_C	(e) σ_i=0.58σ_C	(f)
60°	(a) σ_i=0.61σ_C	(b) σ_i=0.96σ_C	(c) σ_i=σ_C	(d) σ_i=0.87σ_C	(e) σ_i=0.44σ_C	(f)
90°	(a) σ_i=0.55σ_C	(b) σ_i=0.93σ_C	(c) σ_i=σ_C	(d) σ_i=0.90σ_C	(e) σ_i=0.64σ_C	(f)

[a] σ_i is the stress corresponding to the cracking state; σ_C is the UCS of the specimen.

https://doi.org/10.1021/acsomega.3c04849
ACS Omega 2023, 8, 37202−37212

during uniaxial compression. The results of numerical simulations are represented by snapshots (a) to (e). Specifically, snapshots (a) and (b) depict crack propagation prior to reaching the peak, snapshot (c) captures the propagation at the peak, and snapshots (d) and (e) depict the cracking processes occurring after the peak. Snapshot (f) showcases the final state of crack propagation, as observed in the physical tests. In Table 3, the red segments indicate tensile microcracks, while the yellow segments represent shear microcracks. The numbers displayed in snapshots (a−e) indicate the sequence in which the cracks emerge during the numerical tests. For example, numbers 1 and 2 indicate the initiation of the first and second cracks, respectively. The italicized numbers in snapshot (f) indicate the sequence of crack emergence observed in the corresponding laboratory tests. Lowercase letters indicate simultaneous crack initiation within the specimen. It is important to note that the white circles visible in the physical test images correspond to the adhesive marks left by the strain gauges.

4.1. θ = 0°. For a borehole specimen with a bedding inclination of 0°, the first and second cracks, composed of tensile microcracks, initially propagate from the middle of the lower and upper ends of the circular hole toward the loading direction. As the loading continues, two stretch-shear cracking zones (3a,b) emerge at the left and right ends of the circular hole. These zones mainly consist of stretched microcracks (red) and some shear microcracks (yellow). When the load reaches its peak strength, the tensile cracks (4a and 4b) originate from zones 3a and 3b of the tensile-shear crack region and propagate in the loading direction. After the peak strength is reached, when the axial load decreases to 95% of the uniaxial compressive strength (UCS), another tensile crack 5 initiates from zone 3a in the tensile-shear crack region and propagates in the opposite direction to crack 4a. With the continued loading, zones 3a and 3b in the tensile-shear fracture region gradually spread toward the edge of the sample, expanding until the sample undergoes coalescence and experiences complete failure. Snapshots (a)−(e) demonstrate that with increasing load, minimal changes are observed in fracture 1, as it is inhibited by the propagation of fractures 3a, 3b, 4a, and 4b.

From snapshot (f), it is evident that the cracks 1, 2, 3a, and 3b observed in the physical test are successfully replicated in the numerical simulation.

- Cracks 1 and 2 represent the initial cracks that originate from the lower and upper surfaces of the circular hole, respectively.
- Cracks 3a and 3b are secondary cracks that initiate from the left and right sides of the circular hole and propagate in the direction of loading.

4.2. θ = 30°. When the axial load reaches 67% of UCS, the first two cracks (1a and 1b) of the borehole specimen with a bedding angle of θ = 30° initiate from the left and right sides of the circular hole and propagate toward the bottom left and upper right directions, respectively. As the loading progresses, a tensile fracture (crack 2a) initiates from the lower end of the circular hole and propagates in a direction roughly consistent with the bedding inclination. Simultaneously, at the initiation of crack 1b, a tensile fracture propagates (propagates 2b) in the direction of crack 1b propagation. Additionally, two tensile-shear cracking zones (1a and 1b) form at the left and right ends of the circular hole. At the peak load, the tensile-shear fracture zone (1a and 1b) continues to expand toward the left and right edges. Furthermore, a tensile crack (crack 3) also originates from crack 1b and spreads along the edge. After reaching the peak load, additional tensile fractures, such as 4a and 4b, occur, mixing with the macroscopically stretched-shear fracture region until the specimen eventually fails.

It can be observed from the snapshot (f) that cracks 1a, 1b, and 3 captured in the physical test are also reproduced in the numerical simulation.

- Cracks 1a and 1b are the initial cracks that originate from the left and right sides of the circular hole, respectively.
- Crack 3 is the third crack, which initiates from crack 1b and propagates toward the loading direction.

4.3. θ = 45°. When the coal sample with holes has a stratigraphic inclination angle of 45°, the first crack initiates at both ends of the circular hole. As the axial load reaches 89% of that of UCS, two tensile-shear crack regions form at the crack tips. At the peak point, the tensile-shear fracture region gradually expands, and tensile cracks 3a and 3b initiate from 2a and 2b, respectively, propagating along the direction of the bedding inclination angle. After the peak, the tensile crack Section 4a,4b continue to expand until the specimen fails completely.

It can be observed from the snapshot (f) that cracks 1a, 1b, 2a, and 2b captured in the physical test are also replicated in the numerical simulation.

- Cracks 1a and 1b are the initial cracks, originating from the left and right surfaces of the circular hole, respectively.
- Cracks 2a and 2b are the subsequent cracks, originating from cracks 1a and 1b, respectively, and propagating along the direction of the bedding inclination.

4.4. θ = 60°. For the borehole specimen with a bedding angle θ=60°, crack 1 initiates from the left side of the borehole when the axial load reaches 61% of UCS. Subsequently, when the axial load reaches 90%, crack 2 starts from the right end. As the loading process continues, tensile-shear cracking zones 3a and 3b form. Then, crack 4 initiates from 3a and propagates vertically along the bedding direction toward the upper left of the specimen. After the peak, the cracking zone 3b expands and forms a macrotensile cracking zone, which propagates toward the upper right and eventually coalesces with the right edge of the specimen. Simultaneously, a tensile cracking zone 5 initiates and extends toward the lower right.

Comparing the results of the numerical simulation and the laboratory test, we can observe that some key features in the physical test are replicated in the numerical simulation.

- Cracks 1 and 2 are the initial cracks, originating from the left and right surfaces of the circular hole, respectively.
- Crack 5 initiates from the lower right of the circular hole and propagates toward the loading direction.

4.5. θ = 90°. For the borehole specimen with a bedding angle θ = 90°, the cracking process unfolds as follows. Initially, a tensile-shear cracking zone 1 emerges on the left surface of the circular hole. Then, at the right end of the hole, crack 2 initiates. At the load peak, crack 3 extends from crack 2 toward the upper right of the sample. The cracking zone 1 remains almost unchanged thereafter. With further loading, several short tensile cracks appear, connecting these macrotensile-shear cracking zones and contributing to the specimen's failure.

It is evident that some key features observed in the physical test are replicated in the numerical simulation.

- Cracks 1 and 2 are the initial cracks, originating from the upper and lower surfaces of the circular hole, respectively.

https://doi.org/10.1021/acsomega.3c04849
ACS Omega 2023, 8, 37202−37212

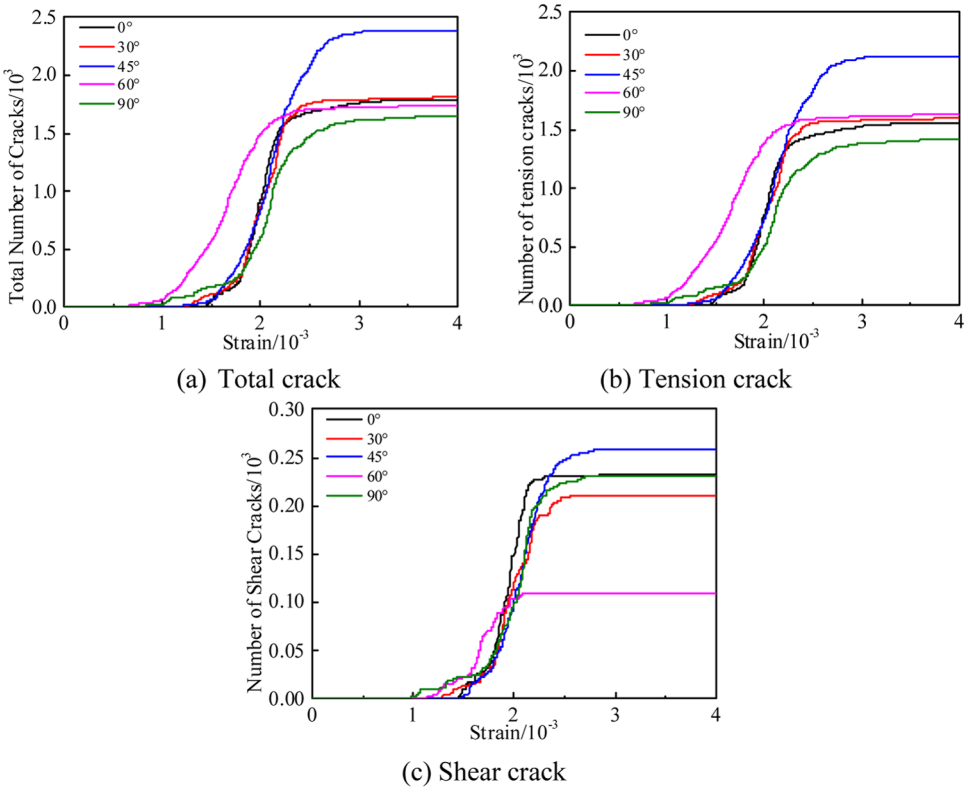

Figure 9. Crack propagation process of the borehole specimen with different bedding angles: (a) total crack; (b) tension crack; (c) shear crack.

By comparison of the cracking processes of specimens with different flaw inclinations, several interesting phenomena can be observed.

(a) As the bedding inclination angle increases, the initiation position of cracks remains largely unchanged, starting from the left and right ends of the circular hole. The ultimate direction of crack propagation aligns closely with the direction of bedding extension. However, for smaller or larger bedding inclination angles (0° or 90°), the direction of crack propagation after initiation shows little correlation with the bedding inclination angle.

(b) As axial strain increases, the crack growth in borehole specimen bodies with different bedding inclination angles exhibits an "S-shaped" curve characterized by a gradual increase, followed by a rapid growth phase, and then a gradual decrease.

(c) The initial failure strength of the borehole specimen with different bedding inclination angles exhibits lower values for tensile failure (peak strength ranging from 30 to 70%) compared to shear failure (peak strength ranging from 55 to 90%). This indicates that the presence of bedding structure contributes to the damage and failure of the borehole specimen body through tensile failure. Moreover, the ratio of tensile cracks (ranging from 85 to 95% of total cracks) is higher than the ratio of shear cracks (ranging from 5 to 15% of total cracks) for different bedding inclination angles, emphasizing that the damage and failure process of the borehole specimen body in the bedding structure is predominantly driven by tensile stress.

(d) As the bedding angle increases, the contribution of shear action to specimen failure gradually decreases, while the contribution of tensile action increases. This observation is supported by Figure 9 and Table 4. The ratio of microtensile cracks to the total number of cracks generally increases with the increase of the bedding angle.

Table 4. Crack Propagation Parameters of a Borehole Specimen with Different Bedding Angles

bedding angle (deg)	total number of cracks	tensile crack ratio (%)	shear crack ratio (%)	initial tension fracture strength σ/σ_{Max} (%)	initial shear failure strength σ/σ_{Max} (%)
0	1811	87.2	12.8	68.1	83.1
30	1818	88.4	11.6	63.8	73.2
45	2391	89.2	10.8	30.5	86.8
60	1752	93.7	6.3	37.3	87.7
90	1660	86.1	13.9	40.6	58.9

5. SPATIOTEMPORAL EVOLUTION OF STRESS FIELD

In Section 4, the cracking process of composite specimens with different dip angles is analyzed. The results indicate that borehole specimens with different bedding inclination angles exhibit distinct cracking mechanisms. Previous studies by Yang et al.[41,42] established a close relationship between the mechanical properties of rock material, the cracking process, and the stress conditions and evolution rules of the stress field.

5.1. Spatial Evolution of the Stress Field. Figure 10 illustrates the stress distribution surrounding the borehole prior to the initiation of the first crack in specimens with varying bedding angles. The figures were drawn based on the local stress values recorded by PFC^{2D} combined with the cubic spline interpolation method.[43] Tensile stress is represented by the

https://doi.org/10.1021/acsomega.3c04849
ACS Omega 2023, 8, 37202−37212

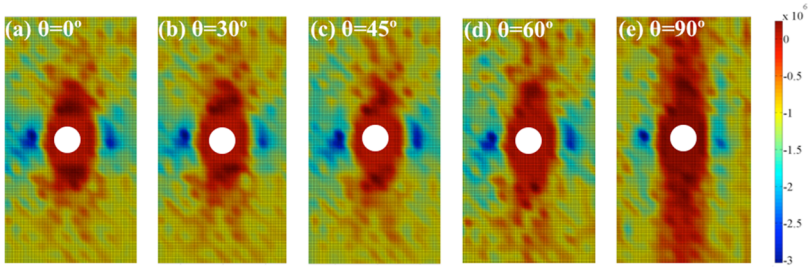

Figure 10. Stress distribution around the borehole with bedding angle θ: (a) $\theta = 0°$; (b) $\theta = 30°$; (c) $\theta = 45°$; (d) $\theta = 60°$; (e) $\theta = 90°$.

color red, while compressive stress is depicted in blue. The brightness of the color indicates the magnitude of the stress. It is evident that the stress distribution conditions differ significantly for specimens with different bedding angles.

From Figure 10, it can be observed that the area of concentrated tensile stress is located in the middle of the sample, while the region of concentrated compressive stress lies on both sides of the borehole. As the bedding inclination increases, the range of the tensile stress concentration area expands toward the top and bottom, while gradually narrowing in width at the middle. The peak area of tensile stress shifts toward the upper and lower ends of the borehole, moving toward the top and bottom of the sample with increasing bedding inclination. At a bedding dip angle of 90°, the tensile stress concentration control zone spans the entire sample. The compressive stress consistently appears on the left and right sides of the borehole with both its range and peak compressive stress remaining relatively unchanged.

5.2. Time Evolution of Stress Field. Considering the similarity in stress evolution around boreholes of coal specimens with different bedding angles over time, we will use an angle of θ = 30° as an example in this study.

Figure 11 illustrates the changing stress distribution around the borehole of a structurally heterogeneous coal body during

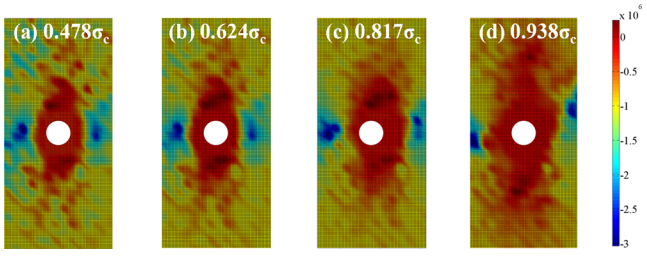

Figure 11. Time evolution of stress field when: (a) σ_i=0.478σ_C; (b) σ_i=0.624σ_C; (c) σ_i=0.817σ_C; (d) σ_i=0.938σ_C.

the loading process. Tensile stress is depicted in red, while compressive stress is represented in blue. The brightness of the color indicates the magnitude of the stress. The snapshots displayed in the figures correspond to the externally applied stresses at each stage of the crack propagation. It is evident that crack propagation alters the stress conditions. As the external load increases, cracks gradually propagate. The concentration area of tensile stress moves to the upper and lower ends of the specimen. Additionally, the range of the concentration area expands over time (or during the cracking process), with the concentration of tensile stress initially increasing and then decreasing over time. In terms of the compression stress concentration area, it is initially situated on the left and right sides of the borehole. As time progresses, it gradually shifts downward on the left and upward on the right, aligning with the direction of the bedding inclination.

6. DISCUSSION

The mechanical properties, crack propagation patterns, and evolution characteristics of the stress field in coal specimens with varying bedding angles were systematically investigated. Nevertheless, there are still some aspects that require further elucidation.

6.1. Crack Initiation Patterns of Coal Specimens with Different Bedding Angles. In this study, we conducted an analysis of the crack initiation, propagation, and coalescence processes in specimens with varying defect slopes (Table 5). It is evident that the starting point and type of crack differ among specimens with different bedding angles. Based on the observed cracking processes in both numerical simulations and laboratory tests, we identified three distinct patterns of crack initiation (as depicted in Figure 12).

To investigate the mechanical basis of the crack initiation mode, the stress field of the specimens prior to the onset of the first crack was studied.

Referring to Figure 12, for specimens with horizontal or vertical bedding angles (θ = 0° or 90°), the central zone of tensile stress exhibits symmetry about the drilling hole. As a result, the crack propagates along the loading direction. In the case of smaller bedding angles (θ = 30°), the central zone of tensile stress demonstrates symmetry in the angle of the bedding

Table 5. Three Types of Crack Initiation Patterns

type	description
type I (a horizontal or vertical specimen of bedding)	the cracks splay toward the top or bottom of the sample from the left and right ends of the borehole. This type of crack initiation pattern can be observed in specimens with bedding inclination of 0 and 90°.
type II (a specimen with a small bedding inclination)	for this type of crack initiation pattern, the cracks start from the left and right ends of the borehole and then propagate along the direction of the bedding inclination angle, respectively. It can be found in specimens with a bedding inclination of 30°.
type III (A specimen with a large bedding inclination)	for this type of crack initiation pattern, the cracks start from the left and right ends of the borehole and propagate in the direction perpendicular to the bedding inclination, and then extend in the direction of the bedding inclination. This type of crack initiation pattern can be observed in specimens with bedding inclination of 45 and 60°.

https://doi.org/10.1021/acsomega.3c04849
ACS Omega 2023, 8, 37202−37212

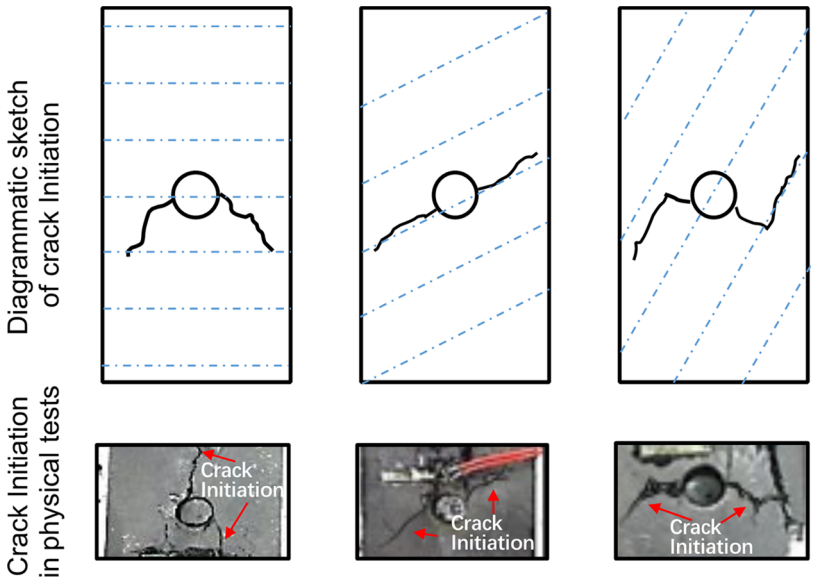

Figure 12. Crack initiation patterns of structural coal specimens with different bedding angles.

inclination direction. Consequently, the crack propagated along the bedding direction. As the bedding angle increases, the peak value of the central zone of tensile stress gradually decreases, while the peak value of the central zone of compressive stress on both sides of the borehole progressively increases. Under the combined influence of these factors, the crack initially propagates along the vertical direction of the bedding inclination for a certain period of time and then extends along the direction of the bedding inclination after the weakening of the compressive stress.

6.2. Influence of Crack Propagation Mode on Mechanical Properties of Specimens. The study presented above focuses on the mechanical properties and crack propagation patterns of structural anisotropic specimens with varying bedding angles. However, the quantitative relationship between these two factors remains unclear.

In this section, the correlation between mechanical properties and crack propagation patterns was investigated by employing quantitative measurements of fractal dimensions in crack propagation patterns.[44,45] For this purpose, Fractal Fox 2.0 software was utilized to calculate the fractal dimensions based on the fundamental definitions of box dimensions. The following calculation formula is employed for this analysis.[32,46]

$$D = \log N(L)/\log(1/L) \quad (1)$$

The formula is defined as follows: L represents the side length of the square grid and $N(L)$ represents the corresponding number of square grids. The specific procedure is as follows: First, the images of crack propagation states were obtained using PFC^{2D} software. Second, the acquired images underwent processing using the binarization method. Subsequently, the processed images were imported into Fractal Fox 2.0, where $\log(L) - \log(1/L)$ curves were generated. The slopes of these curves represent the fractal dimensions of the respective images. Figure 13 depicts the variations in mechanical properties and fractal dimensions of cracks with the changes in peak strength. As the defect inclination increases, both the peak strength and elastic modulus exhibit an upward trend. Conversely, the fractal dimension shows an opposite trend. This can be attributed to the fact that an increased defect inclination results in a simpler

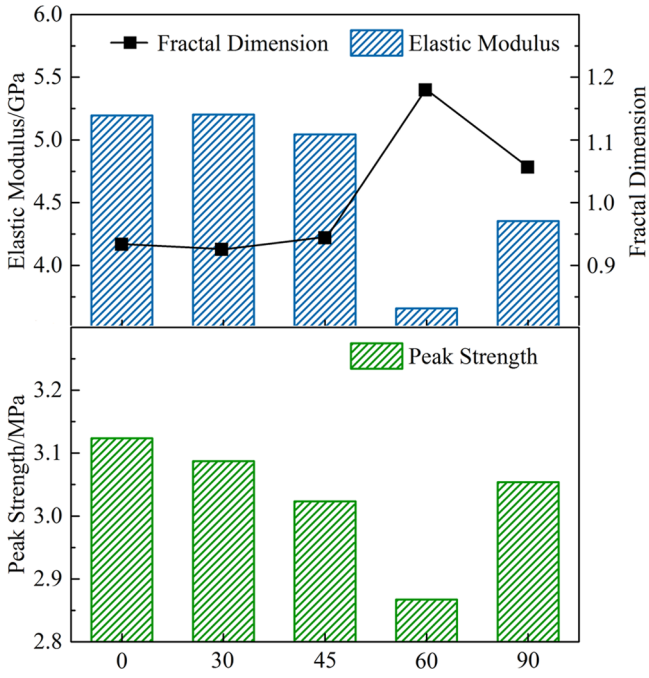

Figure 13. Variation of mechanical properties and fractal dimensions of cracks with the change of peak strength.

fracture propagation mode at the peak point, leading to a smaller corresponding fractal dimension. In other words, a smaller fractal dimension indicates a simpler fracture propagation pattern, implying a lower number of microcracks formed within the sample at the peak. Since the level of damage in a sample is directly proportional to the number of microcracks, it is reasonable to infer that a smaller fractal dimension corresponds to a lower degree of damage.

7. CONCLUSIONS

This study focused on investigating the mechanical properties, crack processes, and stress field evolution of structural anisotropic coal specimens with boreholes during the loading process. Numerical simulations were employed, and physical

https://doi.org/10.1021/acsomega.3c04849
ACS Omega 2023, 8, 37202−37212

tests were conducted to validate the numerical findings. Remarkably, a strong consistency was observed between the numerical and physical test results.

During the crack growth process, it was observed that the uniaxial compressive strength and elastic modulus of the structural anisotropic specimens with boreholes initially decreased and then increased with an increase in the bedding inclination. Both trends exhibited nonlinear characteristics.

The analysis of the crack propagation process revealed that varying the bedding inclination led to different modes of crack propagation. As the bedding angle increased, the crack propagation pattern gradually changed and three distinct crack initiation patterns were identified. Moreover, the number of discrete microcracks exhibited an initial decrease, followed by an increase with an increase in bedding inclination angle. Furthermore, it was observed that the contribution of shear action to specimen failure gradually decreased, while the contribution of tensile action increased with an increasing bedding inclination angle. These findings provide valuable scientific guidance for gas extraction in coal seams with different bedding angles.

■ ASSOCIATED CONTENT

Data Availability Statement

The data used to support the findings of this study are available from the corresponding author upon request.

■ AUTHOR INFORMATION

Corresponding Author

Nan Liu − *College of Quality and Safety Engineering, China Jiliang University, Hangzhou 310018, China;* orcid.org/0000-0002-9717-2137; Phone: +86-152-0161-9572; Email: liunan@cjlu.edu.cn

Authors

Chang Guo − *College of Quality and Safety Engineering, China Jiliang University, Hangzhou 310018, China; School of Safety Engineering, China University of Mining and Technology, Xuzhou 221116, China*

Zedong Wang − *College of Quality and Safety Engineering, China Jiliang University, Hangzhou 310018, China*

Ting Liu − *School of Safety Engineering, China University of Mining and Technology, Xuzhou 221116, China*

Baiquan Lin − *School of Safety Engineering, China University of Mining and Technology, Xuzhou 221116, China*

Chuanjie Zhu − *School of Safety Engineering, China University of Mining and Technology, Xuzhou 221116, China*

Zhanbo Huang − *School of Safety Engineering, China University of Mining and Technology, Xuzhou 221116, China*

Complete contact information is available at: https://pubs.acs.org/10.1021/acsomega.3c04849

Author Contributions

C.G. conducted the experiments, analyzed the results, and wrote the final manuscript. Z.W. designed and performed the numerical simulations. T.L. and C.Z. contributed in analysis of the results. B.L. was the main supervisor of the research. Z.H. performed the experiment and discussion of the results. N.L. contributed in reviewing and editing the manuscript.

Funding

This work was supported by the Natural Science Foundation of Zhejiang Province (LQ21E040005) and the National Natural Science Foundation of China (52204247, 12302448).

Notes

The authors declare no competing financial interest.

■ ACKNOWLEDGMENTS

The authors would like to thank editors and reviewers for their constructive comments that helped the authors to enhance overall quality of the manuscript.

■ REFERENCES

(1) Laubach, S. E.; Marrett, R. A.; Olson, J. E.; Scott, A. R. Characteristics and origins of coal cleat: A review. *Int. J. Coal Geol.* **1998**, *35* (1), 175−207.

(2) Yang, W.; Wang, W.; Jia, R.; Walton, G.; Sinha, S.; Chen, Q.; Lin, B.; Jiao, X. Parameter optimization of coal face blasting for coal and gas outburst control. *Bull. Eng. Geol. Environ.* **2023**, *82*, No. 80.

(3) Zou, Q.; Chen, Z.; Cheng, Z.; Liang, Y.; Xu, W.; Wen, P.; Zhang, B.; Liu, H.; Kong, F. Evaluation and intelligent deployment of coal and coalbed methane coupling coordinated exploitation based on Bayesian network and cuckoo search. *Int. J. Min. Sci. Technol.* **2022**, *32* (6), 1315−1328.

(4) Wei, G.; Wen, H.; Deng, J.; Ma, L.; Li, Z.; Lei, C.; Fan, S.; Liu, Y. Liquid CO2 injection to enhance coalbed methane recovery: An experiment and in-situ application test. *Fuel* **2021**, *284*, No. 119043.

(5) Szlązak, N.; Obracaj, D.; Swolkień, J. Methane drainage from roof strata using an overlying drainage gallery. *Int. J. Coal Geol.* **2014**, *136*, 99−115.

(6) Zhou, F.; Xia, T.; Wang, X.; Zhang, Y.; Sun, Y.; Liu, J. Recent developments in coal mine methane extraction and utilization in China: a review. *J. Nat. Gas Sci. Eng.* **2016**, *31*, 437−458.

(7) Kędzior, S.; Dreger, M. Time variability of methane extraction from hard coal deposits in the Upper Silesian Coal Basin (Poland) in relation to geological and mining conditions. *J. Sustainable Min.* **2023**, *22* (2), 89−99.

(8) Gerami, A.; Mostaghimi, P.; Armstrong, R. T.; Zamani, A.; Warkiani, M. E. A microfluidic framework for studying relative permeability in coal. *Int. J. Coal Geol.* **2016**, *159*, 183−193.

(9) Zheng, C.; Jiang, B.; Xue, S.; Chen, Z.; Li, H. Coalbed methane emissions and drainage methods in underground mining for mining safety and environmental benefits: A review. *Process Saf. Environ. Prot.* **2019**, *127*, 103−124.

(10) Pan, R.; Cheng, Y.; Yuan, L.; Yu, M.; Dong, J. Effect of bedding structural diversity of coal on permeability evolution and gas disasters control with coal mining. *Nat. Hazards* **2014**, *73* (2), 531−546.

(11) Feng, Z.; Zhou, D.; Zhao, Y.; Cai, T. Study on microstructural changes of coal after methane adsorption. *J. Nat. Gas Sci. Eng.* **2016**, *30*, 28−37.

(12) Wang, Y.; Yang, R. Study of the dynamic fracture characteristics of coal with a bedding structure based on the NSCB impact test. *Eng. Fract. Mech.* **2017**, *184* (15), 319−338.

(13) Huang, B.; Cheng, Q.; Chen, S. Phenomenon of methane driven caused by hydraulic fracturing in methane-bearing coal seams. *Int. J. Min. Sci. Technol.* **2016**, *26* (5), 919−927.

(14) Pan, R.; Fu, D.; Yu, M. G.; Chen, L. Directivity effect of unloading bedding coal induced fracture evolution and its application. *Int. J. Min. Sci. Technol.* **2017**, *27* (5), 825−829.

(15) Tan, L.; Ren, T.; Yang, X.; He, X. A numerical simulation study on mechanical behaviour of coal with bedding planes under coupled static and dynamic load. *Int. J. Min. Sci. Technol.* **2018**, *28* (5), 791−797.

(16) Zhao, Y.; Zhao, Y.; Jiang, Y.; Elsworth, D.; Huang, Y. Effects of bedding on the dynamic indirect tensile strength of coal: Laboratory experiments and numerical simulation. *Int. J. Coal Geol.* **2014**, *132*, 81−93.

(17) Liu, X.; Dai, F.; Zhang, R.; Liu, J. Static and dynamic uniaxial compression tests on coal rock considering the bedding directivity. *Environ. Earth Sci.* **2015**, *73* (10), 5933−5949.
(18) Hao, X.; Du, W.; Jiang, Y.; Tannant, D.; Zhao, Y.; Guo, Y. Influence of bedding and cleats on the mechanical properties of a hard coal. *Arabian J. Geosci.* **2018**, *11* (9), No. 200.
(19) Seedsman, R. W. Geotechnical sedimentology—its use in underground coal mining. *Int. J. Coal Geol.* **2001**, *45* (2), 147−153.
(20) Peng, S.; Fang, Z.; Shen, J.; Xu, J.; Wang, G. Effects of gas sorption-induced swelling/shrinkage on the cleat compressibility of coal under different bedding directions. *Sci. Rep.* **2017**, *7* (1), No. 14337.
(21) Li, Q.; Zhao, Z.; Liu, P.; Nie, B.; Zhao, Y.; Liu, X.; Deng, B.; Wang, M. Evaluation of structural damage and gas transportability change in coal subjected to ultrasound stimulation using image-based modeling and permeability tests. *Fuel* **2023**, *349*, No. 128684.
(22) Harrison, J. P.; Hudson, J. A.; Popescu, M. E. Engineering Rock Mechanics: Part 2. Illustrative Worked Examples. *Appl. Mech. Rev.* **2002**, *55* (2), B30−B31.
(23) Takanashi, M.; Nishizawa, O.; Kanagawa, K.; Yasunaga, K. Laboratory measurements of elastic anisotropy parameters for the exposed crustal rocks from the Hidaka Metamorphic Belt, Central Hokkaido, Japan. *Int. J. Rock Mech. Min. Sci.* **2001**, *145* (1), 33−47.
(24) Jaeger, J. C. Shear failure of anisotropic rocks. *Geol. Mag.* **1960**, *97* (1), 65−72.
(25) Cazacu, O.; Cristescu, N. D.; Shao, J. F. A new failure criterion for transversely isotropic rocks. *Int. J. Rock Mech. Min. Sci.* **1998**, *35* (4), 421−435.
(26) Hoek, E.; Brown, E. T. Practical estimates of rock mass strength. *Int. J. Rock Mech. Min. Sci.* **1997**, *34* (34), 1165−1186.
(27) Shi, X.; Yang, X.; Meng, Y.; Li, G. An anisotropic strength model for layered rocks considering planes of weakness. *Rock Mech. Rock Eng.* **2016**, *49*, 3783−3792.
(28) Alexeev, A. D.; Revva, V. N.; Alyshev, N. A.; Zhitlyonok, D. M. True triaxial loading apparatus and its application to coal outburst prediction. *Int. J. Coal Geol.* **2004**, *58* (4), 245−250.
(29) Okubo, S.; Fukui, K.; Qingxin, Q. I. Uniaxial compression and tension tests of anthracite and loading rate dependence of peak strength. *Int. J. Coal Geol.* **2006**, *68* (3−4), 196−204.
(30) Song, H.; Jiang, Y.; Elsworth, D.; Zhao, Y.; Wang, J.; Liu, B. Scale effects and strength anisotropy in coal. *Int. J. Coal Geol.* **2018**, *195*, 37−46.
(31) Potyondy, D. O.; Cundall, P. A. A bonded-particle model for rock. *Int. J. Rock Mech. Min. Sci.* **2004**, *41* (8), 1329−1364.
(32) Liu, T.; Lin, B.; Yang, W.; Wei, Y.; Zou, Q.; Kong, J.; Yan, F. Cracking Process and Stress Field Evolution in Specimen Containing Combined Flaw Under Uniaxial Compression. *Rock Mech. Rock Eng.* **2016**, *49*, 3095−3113.
(33) Wang, T.; Zhou, W.; Chen, J.; Xiao, X.; Li, Y.; Zhao, X. Simulation of hydraulic fracturing using particle flow method and application in a coal mine. *Int. J. Coal Geol.* **2014**, *121* (Complete), 1−13.
(34) Liu, T.; Lin, B.; Zheng, C.; Zou, Q.; Zhu, C.; Yan, F. Influence of coupled effect among flaw parameters on strength characteristic of precracked specimen: application of response surface methodology and fractal method. *J. Nat. Gas Sci. Eng.* **2015**, *26* (Complete), 857−866.
(35) Zhang, X.-P.; Wong, L. Loading rate effects on cracking behavior of flaw-contained specimens under uniaxial compression. *Int. J. Fract.* **2013**, *180*, 93−110.
(36) Itasca, C. G. *Users' Manual for Particle Flow Code in 2dimensions (PFC2D)*; Version 3.1. Itasca Consulting Group Inc.: Minneapolis Minnesota, 2002.
(37) Chen, X.; Liao, Z.; Peng, X. Deformability characteristics of jointed rock masses under uniaxial compression. *Int. J. Min. Sci. Technol.* **2012**, *22* (2), 213−221.
(38) Lee, H.; Jeon, S. An experimental and numerical study of fracture coalescence in pre-cracked specimens under uniaxial compression. *Int. J. Solids Struct.* **2011**, *48* (6), 979−999.
(39) Yang, S.; Dai, Y.; Han, L.; Jin, Z. Experimental study on mechanical behavior of brittle marble samples containing different flaws under uniaxial compression. *Eng. Fract. Mech.* **2009**, *76* (12), 1833−1845.
(40) Zhang, X. P.; Wong, L. Crack Initiation, Propagation and Coalescence in Rock-Like Material Containing Two Flaws: a Numerical Study Based on Bonded-Particle Model Approach. *Rock Mech. Rock Eng.* **2013**, *46*, 1001−1021.
(41) Yang, S.-Q.; Huang, Y.; Jing, H.; Liu, X. Discrete element modeling on fracture coalescence behavior of red sandstone containing two unparallel fissures under uniaxial compression. *Eng. Geol.* **2014**, *178* (21), 28−48.
(42) Yang, S. Q.; Jing, H. W.; Xu, T. Mechanical behavior and failure analysis of brittle sandstone specimens containing combined flaws under uniaxial compression. *J. Cent. South Univ.* **2014**, *21*, 2059−2073.
(43) Liu, T.; Lin, B. Q.; Yang, W. Mechanical behavior and failure mechanism of pre-cracked specimen uniaxial compression. *Tectonophysics* **2017**, *712*−*713*, 330−343.
(44) Li, H.-Q.; Wong, L. N. Y. Numerical Study on Coalescence of Pre-Existing Flaw Pairs in Rock-Like Material. *Rock Mech. Rock Eng.* **2014**, *47* (6), 2087−2105.
(45) Zhao, Y. Crack pattern evolution and a fractal damage constitutive model for rock. *Int J Rock Mech Min Sci* **1998**, *35* (3), 349−366.
(46) Zhao, D.; Zheng, M. Fractal characteristics of cracks and fragments generated in unloading rockburst tests. *Int. J. Min. Sci. Technol.* **2014**, *24* (6), 819−823.

https://doi.org/10.1021/acsomega.3c04849
ACS Omega 2023, 8, 37202−37212